

# Source properties of the 29 January 2011 $M_L$ 4.5 Oroszlány (Hungary) mainshock and its aftershocks

Zoltán Wéber and Bálint Süle

Kövesligethy Radó Seismological Observatory,  
MTA CSFK GGI, H-1112 Budapest, Meredek u. 18., Hungary.

E-mail: [weber@seismology.hu](mailto:weber@seismology.hu); [suba@seismology.hu](mailto:suba@seismology.hu)

---

*Accepted manuscript published in*

**Bulletin of the Seismological Society of America, Vol. 104, No. 1, pp. 113-127,  
February 2014, doi: 10.1785/0120130152**

## Abstract

In the most seismically active region of Hungary, an earthquake of  $M_L$  4.5 occurred near the town of Oroszlány on 29 January 2011. The mainshock was followed by more than 200 aftershocks. This event is the first earthquake in the country above  $M_L$  4 that was recorded on a significant number of three-component digital seismic stations. According to the inversion of arrival times, the hypocenter of the mainshock was at a depth of about 5 km near Oroszlány with horizontal errors of about 1.5 km. The aftershocks were confined to a small region next to the mainshock. For the main event, we obtained an average moment magnitude of  $M_w = 4.2$ , P- and S-wave source radii of  $r^P = 970$  m and  $r^S = 972$  m, and static stress drops of  $\Delta\sigma^P = 6.67 \times 10^5$  Pa and  $\Delta\sigma^S = 17.60 \times 10^5$  Pa from the analysis of P- and S-wave displacement spectra, respectively. The retrieved spectral source parameters for the investigated events agree well with the results of earlier research. We have also shown that our local waveform inversion method applied in this study is suitable to estimate the earthquake source mechanism for low-magnitude events using local waveforms exclusively. The moment tensor computed for the mainshock from local waveform data shows a strike-slip mechanism with a north–south-striking and an east–west-striking nodal plane, agreeing well with regional moment tensor solutions of other agencies. The source mechanisms of four aftershocks with  $M_L \geq 2$  were also successfully estimated. Three of

them had strike-slip mechanism very similar to that of the mainshock, whereas the fourth one was a thrust faulting event with some strike-slip component. The sub-horizontal P-axis struck about north-east–south-west for both the mainshock and all the analyzed aftershocks, coinciding with the general trend of the compressional stress field in the epicentral region.

## Introduction

In the central part of the Pannonian basin (mainly occupied by Hungary), seismic activity can be characterized as moderate. The seismicity pattern in Hungary shows that earthquakes are restricted to the upper part of the crust and the control by pre-existing fault zones is strongly masked by the random hypocentral distribution due to the general weakness of the lithosphere. However, there are certain areas where the likelihood of earthquake occurrence is higher and where significant, destructive earthquakes occurred in the last centuries. The most notable events are the M6.2 Komárom (1763,  $I = 8.5$ ), the M5.4 Mór (1810,  $I = 8$ ), the M5.6 Kecskemét (1911,  $I = 8$ ), the M5.3 Eger (1925,  $I = 7.5$ ), the M5.6 Dunaharaszti (1956,  $I = 8$ ), the M4.9 Berhida (1985,  $I = 7$ ), and the M4.5 Oroszlány (2011,  $I = 6$ ) earthquakes (Zsíros, 2000) (Fig. 1). Statistical studies show that four to five 2.5-3.5 magnitude earthquakes can be expected every year in the country, which can be felt near the epicenter, but cause no damage (Tóth *et al.*, 2002). Events causing light damage occur every 15-20 years, whereas stronger, more damaging ( $M = 5.5 - 6$ ) quakes happen about every 40-50 years.

The Berhida - Mór - Komárom (BMK) region in north-west Hungary (Fig. 1) is the most seismically active zone of the country. In the last 250 years, four significant earthquakes occurred in this area. Moreover, numerous small-magnitude earthquakes indicate that seismic activity is persistent. From neotectonic point of view, this seismogenic zone is part of the region where the 1.2-1.3 mm/year movement of the East Alpine–Northwest Pannonian crustal unit towards north-east direction decreases and many poorly constrained structural elements exist there (Grenerczy *et al.*, 2000, 2005; Fodor *et al.*, 2005).

In the seismically active BMK region, an earthquake of local magnitude  $M_L$  4.5 occurred near the town of Oroszlány on the 29th of January, 2011. The earthquake was strongly felt in Oroszlány and neighboring villages, where it caused minor damage. The earthquake was also felt further away across northwestern Hungary, even in the capital city of Budapest. Before the end of March, the

mainshock was followed by more than 200 aftershocks, four of which having  $M_L \geq 2$ . The largest aftershock had a magnitude of  $M_L$  2.7. The macroseismic intensity of the main event was as large as 6 on the European Macroseismic Scale.

Since the middle of the 1990s, several digital seismological stations have been installed in Hungary. At the time of the Oroszlány earthquake, a total of 6 permanent broad-band stations and 9 short-period ones were operational in Hungary. This event is, therefore, the first earthquake in the country above local magnitude  $M_L$  4 that was recorded on a significant number of three-component digital seismographs. Here we utilize these data in the analysis of the mainshock and its aftershocks. Two temporary short-period stations were also deployed after the main event in order to better record the aftershocks.

In this paper we analyze all seismic data available to us for the Oroszlány mainshock and its aftershocks in order to (1) determine their hypocenter locations by the inversion of arrival times; (2) estimate their scalar moments, source radii and static stress drops from spectral analysis and (3) determine the source mechanism (full moment tensor) of the main event and the  $M_L \geq 2$  aftershocks using local waveform inversion. Reliable knowledge of earthquake source properties is essential to better understand the present-day tectonic processes characteristic to the source area. The available data set also presents us with an opportunity to show that our recently developed local waveform inversion method (Wéber, 2006, 2009) is suitable to estimate the earthquake source mechanism for low-magnitude local events.

## Data

At the time of the Oroszlány earthquake, the Hungarian National Seismological Network (HNSN) operated by the Kövesligethy Radó Seismological Observatory (KRSO) comprised 6 permanent broad-band stations and 2 short-period ones. Moreover, we had access to the data of 7 additional short-period stations that were part of the Paks Microseismic Monitoring Network (PMMN) (Fig. 1).

The broad-band stations were equipped with three-component Streckeisen STS-2 seismometers with natural period of 120 s, whereas the HNSN short-period stations used three-component Kinematics SS-1 sensors with natural frequency of 1 Hz. At the PMMN stations three-component 1 Hz Lennartz LE-3D geophones were deployed.

Between the 1st of February and the 13th of April, 2011, two temporary stations (BOKD and

VSOM, Fig. 1) were also operated by the KRSO in cooperation with the Eötvös Loránd Geophysical Institute (ELGI) in order to better record the aftershocks. These short-period stations were equipped with Reftek L4 seismometers with natural frequency of 2 Hz. Just as important, seismological data were also available from the neighboring countries and international agencies.

## Hypocenter location

The mainshock was well recorded on seismic stations across Hungary, and also across eastern and central Europe. The nearest recording station was PKSG (Gánt), only about 8 kilometers from the epicenter (Fig. 1). The greatest aftershocks were also detected by most stations in the country, and after the deployment of the two temporary stations BOKD and VSOM, many small events were recorded by at least four seismographs.

We manually picked P-wave arrival times from vertical-component data and S-wave arrival times from horizontal-component data where possible. For estimating hypocentral locations, we considered those events only that had at least four P-wave and four S-wave time readings. Data from seismic stations with epicentral distance greater than about 300 km were not taken into account in the localization procedure. After applying these selection criteria, a total of 22 P- and 11 S-wave arrivals were used for locating the mainshock and we found 67 aftershocks with the desired number of high-quality arrival time data.

The hypocentral locations were computed using the probabilistic non-linear NonLinLoc software package (Lomax *et al.*, 2000). We employed the oct-tree importance sampling algorithm to map the posterior probability density function (PPDF) of the earthquake location completely and efficiently (Lomax and Curtis, 2001). For constructing the PPDF, we applied the Equal Differential Time (EDT) likelihood function. The main advantage of this formalism is that because the PPDF depends neither on the estimate of origin time nor on the residual root mean square, residual outliers are objectively detected and cleaned out from the original data set without any iterative process or subjective weighting (Font *et al.*, 2004). For calculating theoretical travel times, we used a recently developed one-dimensional (1D) velocity model (Table 1) constructed from arrival time data of earthquakes and controlled explosions for the territory of Hungary (Gráczer and Wéber, 2012).

In the localization procedure, we performed two runs of NonLinLoc. After the first run, using the resulting arrival time residuals for all event–station pairs, we calculated the average residuals for

both the P-waves and the S-waves at each station. Then, for the second run, we used these average residuals as station corrections to achieve the final hypocentral locations (see the NonLinLoc manual). The hypocentral parameters of the mainshock and the selected 67 aftershocks are summarized in Table 2 and in Figs 2 and 3.

Fig. 2 shows the epicenter of the mainshock and its 90 per cent confidence ellipse, together with the scatter density plot of the resulting hypocenter PPDF. The figure demonstrates that the solution is somewhat better constrained in the west-east direction than in the north-south one. The estimated horizontal errors are of the order of 1.5 km. Our solution is situated within a few kilometers from the solutions given by the U.S. Geological Survey (USGS) National Earthquake Information Center (NEIC), the European-Mediterranean Seismological Centre (EMSC), the International Seismological Centre (ISC), as well as the KRSO (Gráczner *et al.*, 2012). We consider our solution to be better, as it is based on more local stations, careful phase picking, and a recent local velocity model.

The hypocentral depth was estimated at 5.1 km with a 90 per cent confidence of 1.6 km. Generally, depth determination requires one or more stations with epicentral distance less than twice the event depth, which is the case here. The relatively small uncertainty in the event depth may be attributed to this favorable condition.

Fig. 3 depicts the epicentral distribution of the mainshock and its selected 67 aftershocks as published in the Hungarian National Seismological Bulletin (HNSB, Gráczner *et al.*, 2012) and as determined in this study. Epicenters estimated by routine observatory data processing show high scatter and an apparent linear trend can be observed in their distribution. Our solutions, on the other hand, are confined to a small region of a few squared kilometers and their distribution does not show any particular trend. Considering the size of the resulting epicentral error ellipses we can safely conclude that the earthquakes studied in this paper occurred practically in the same small-scale seismogenic zone.

The focal depths of the aftershocks are mainly confined to the region of 6–8 km. For events that occurred before the deployment of the temporal seismic stations BOKD and VSOM (Fig. 1), the obtained epicenters are generally better constrained in the west-east direction than in the north-south one. On the other hand, after installing the two stations on 1 February, the reliability of the retrieved epicentral coordinates increased considerably, especially in the north–south direction (Table 2).

## Spectral source parameters

In this section we invert the displacement spectra of P- and S-wave seismograms for low-frequency spectral level and, when possible, corner frequency using the standard Brune’s model (Brune, 1970). Then we compute seismic moment, source dimension, and static stress drop of the analyzed events. Our data set consists of the mainshock and 24 aftershocks with sufficient signal-to-noise ratio. We follow the methodology described in Süle and Wéber (2013).

After instrumental correction, the observed displacement amplitude spectrum  $U(f, R)$  at a hypocentral distance  $R$  can be described as

$$U(f, R) = G(R) \cdot A(f, t) \cdot S(f) \quad (1)$$

where  $f$  is the frequency,  $t$  the travel time,  $G(R)$  the attenuation due to geometrical spreading,  $A(f, t)$  the anelastic attenuation, and  $S(f)$  the amplitude source spectrum. Anelastic attenuation can be divided into two parts. The first term describes the path-dependent attenuation with  $Q(f)$  being the frequency-dependent quality factor, whereas the second term is the near-surface attenuation characterized by the  $\kappa$  parameter (Singh *et al.*, 1982):

$$A(f, t) = \exp\left(-\frac{\pi f t}{Q(f)}\right) \cdot \exp(-\pi f \kappa) \quad (2)$$

In this study we used the average attenuation models of  $Q_P(f) = 154f^{0.92}$  and  $Q_S(f) = 77f^{0.92}$  for P- and S-waves, respectively (Süle and Wéber, 2013).

Near-surface attenuation can be estimated from seismic waveforms recorded at short hypocentral distances, where the path-dependent attenuation in equation (2) is not significant (Havskov *et al.*, 2003; Havskov and Ottemöller, 2010). For frequencies below the corner frequency,  $\kappa$  can be determined from the slope of the displacement spectrum plotted in a semi-logarithmic diagram. For estimating near-surface effects, we selected all the available event-station pairs from our data set for which epicentral distance is less than 25 km and the event size is small enough to have a corner frequency as high as possible. This latter criteria is necessary for performing reliable data fitting in the usable frequency range. After analyzing 34 seismograms of two stations, we obtained  $\kappa$  values between 0.01 and 0.04 s with a mean of  $0.016 \pm 0.013$  s for P-waves and between 0.02 and 0.04 s with

a mean of  $0.026 \pm 0.008$  s for S-waves. These values are slightly smaller than those determined as an average for the whole territory of Hungary (Süle and Wéber, 2013), probably because the seismic stations used in the present study are all installed on hard limestone.

After correcting for anelastic attenuation and geometrical spreading, the displacement amplitude spectrum  $U_{corr}(f)$  can be written as

$$U_{corr}(f) = \frac{A_0}{1 + \left(\frac{f}{f_c}\right)^2} \quad (3)$$

where the term on the right-hand side is the amplitude source spectrum with low-frequency spectral level  $A_0$  and corner frequency  $f_c$  (Brune, 1970; Hanks and Wyss, 1972). Considering P- and S-wave data separately, after estimating the spectral parameters  $A_0$  and  $f_c$  by a grid search algorithm, we first calculated the scalar seismic moment ( $M_0^P$  and  $M_0^S$ ) for each event-station pair. Then, for each event, the average values and the multiplicative error factors for the seismic moment and corner frequency were computed. Calculations were made using P- and S-wave data separately, following the equations proposed by Archuleta *et al.* (1982):

$$\bar{x} = \text{alog} \left( \frac{1}{N} \sum_{i=1}^N \log x_i \right) \quad (4)$$

$$\text{StDev}[\log \bar{x}] = \left( \frac{1}{N-1} \sum_{i=1}^N (\log x_i - \log \bar{x})^2 \right)^{1/2} \quad (5)$$

$$E\bar{x} = \text{alog}(\text{StDev}[\log \bar{x}]) \quad (6)$$

where  $x$  stands for  $M_0^{P,S}$  or  $f_c^{P,S}$ ,  $\bar{x}$  denotes the mean of  $x$ ,  $N$  is the number of the stations used,  $\text{StDev}[\cdot]$  is the standard deviation of the argument, and  $E\bar{x}$  is the multiplicative error factor for  $\bar{x}$ .

We also computed the moment magnitude  $M_w$  from the average seismic moment  $M_0$  (computed as the logarithmic mean of the  $M_0^P$  and  $M_0^S$  values) according to the definition of Hanks and Kanamori (1979):

$$M_w = \frac{2}{3} \log M_0 - 6.03 \quad (7)$$

where  $M_0$  is measured in Nm. All of the average source parameters and the multiplicative error factors, along with the moment magnitudes, are listed in Table 3. Unfortunately, for 13 low-magnitude aftershocks, the estimation of  $f_c$  was unsuccessful due to the high corner frequency and the insuffi-

cient sampling rate.

For the mainshock, we obtained seismic moments of  $M_0^P = 1.38 \times 10^{15}$  Nm and  $M_0^S = 3.68 \times 10^{15}$  Nm with an average moment magnitude of  $M_w = 4.2$ . The retrieved corner frequencies are  $f_c^P = 1.9$  Hz and  $f_c^S = 1.3$  Hz, the source radii are  $r^P = 970$  m and  $r^S = 972$  m, and the static stress drops are  $\Delta\sigma^P = 6.67 \times 10^5$  Pa and  $\Delta\sigma^S = 17.60 \times 10^5$  Pa.

Recently, Süle and Wéber (2013) have spectrally analyzed 50 earthquakes that occurred in Hungary. Their data set can be significantly expanded in the low-magnitude range with the results obtained in the present study. The new data do not change the observed trends and conclusions published previously. The following remarks refer to the combination of the two data sets.

Generally,  $M_0^P$  is slightly smaller than  $M_0^S$ : the logarithmic mean of the  $M_0^P/M_0^S$  ratio is 0.97. Broadly speaking, corner frequency decreases with increasing seismic moment and  $f_c^P$  is basically larger than  $f_c^S$ , with an average ratio of  $1.59 \pm 0.54$ . The retrieved source radii have an average  $r^P/r^S$  ratio of  $1.04 \pm 0.38$ . Inspecting Fig. 4 it can be observed that source radius increases with increasing moment. The obtained relations for  $r$  versus  $M_0$  are:

$$\log r^P = (0.27 \pm 0.03) \cdot \log M_0^P - (1.02 \pm 0.33) \quad (8)$$

and

$$\log r^S = (0.24 \pm 0.02) \cdot \log M_0^S - (0.72 \pm 0.31) \quad (9)$$

with correlation coefficients of 0.83 and 0.82, respectively. If self-similarity holds, it follows that  $\log r \propto 1/3 \cdot \log M_0$ . The slopes of the regression lines in equations (8) and (9) are clearly smaller than the theoretical value of  $1/3$ , especially in the case of S-waves. At the same time, the correlation coefficients between seismic moment and static stress drop are very low: only 0.35 for P-waves and 0.48 for S-waves. Based on these observations and taking into consideration the high scatter of our data, the breakdown of self-similarity is not found.

In Fig. 5 moment magnitude is plotted against local magnitude. Local magnitudes were estimated according to the formula given by Bakun and Joyner (1984):

$$M_L = \log(A) + 1.00 \cdot \log(D) + 0.00301 \cdot D - 1.99 \quad (10)$$



where  $D$  is the epicentral distance in kilometers and  $A$  is the largest S-wave amplitude measured in nanometers on a ground displacement seismogram that has been filtered with the response of a Wood-Anderson seismograph. As Fig. 5 illustrates, the magnitude values for the Oroszlány mainshock and its aftershocks integrate well into the earlier results. The least-squares fit to the extended data set yields

$$M_w = (0.73 \pm 0.02) \cdot M_L + (0.86 \pm 0.05) \quad (11)$$

with a rather high correlation coefficient of 0.98. The obtained regression line is in good agreement with that suggested by Süle and Wéber (2013).

## Source mechanism

In this section we estimate the source mechanism (full moment tensor) of the Oroszlány mainshock and its four aftershocks with local magnitude  $M_L \geq 2$ . We first briefly summarize the probabilistic non-linear local waveform inversion procedure employed in this study. Then we investigate the main event in detail and show that the applied inversion method is suitable to determine the moment tensor of local events with sufficient reliability. Finally, the four selected aftershocks are analyzed.

## Method

The waveform inversion method we applied to determine the seismic moment tensor has been developed by Wéber (2006, 2009). It works in the point source approximation and is summarized briefly in the following paragraphs.

We describe a general seismic point source by six independent moment tensor rate functions (MTRFs). MTRF description of an earthquake allows the moment tensor to vary arbitrarily as a function of time. If the Green’s functions (GFs), i.e. the velocity structure and hypocentral location are known, there is a linear connection between the seismograms and the MTRFs. Basically, the MTRFs are obtained by deconvolving the GFs from the observed seismograms. For the generation of the synthetic GFs, we employed a propagator matrix–wavenumber integration method (Wang and Herrmann, 1980; Herrmann and Wang, 1985), which allows us to calculate the entire wavefield for horizontally layered earth structures. In this study, we used the same 1D velocity model as that used for earthquake localization (Table 1).

In case of short epicentral distances, however, routinely determined hypocenters are usually not accurate enough to be used in focal mechanism inversion. Therefore, we must consider hypocentral coordinates as unknown parameters that makes the waveform inversion problem non-linear.

In the first step of our waveform inversion procedure, we use the hypocenter estimated by the NonLinLoc software as *a priori* information and the observed waveforms as data to map the PPDF of the hypocenter using the oct-tree importance sampling algorithm (Lomax and Curtis, 2001). As a result we get a large number of hypocentral solutions that are samples from the PPDF. Given these samples, several statistical properties of the hypocentral coordinates can be determined, such as the maximum likelihood point, the mean, the median, etc. For all hypocentral locations, the MTRFs are calculated as well. Their distribution represents the uncertainty of the MTRFs due to that of the hypocenter.

Measurement errors and modeling errors also lead to MTRF uncertainty even for a fixed source position. To estimate the overall uncertainties of the retrieved MTRFs, we use a Monte Carlo simulation technique (Rubinstein and Kroese, 2008). The procedure takes into account the effects of the random noise contained in the seismograms, the uncertainty of the hypocenter determined in the previous step, and the inaccurate knowledge of the velocity structure. By simulating the uncertainty of both the hypocenter and waveforms, in the second step of the waveform inversion, a large number of MTRF solutions is obtained that can be considered as samples from the PPDF of the MTRF. Then statistical properties, such as the maximum likelihood point, the mean, or the median, can be deduced.

Assuming that the focal mechanism is constant in time, in the third step of our waveform inversion method, we decompose the previously obtained MTRFs into a time-invariant moment tensor and a source time function (STF). The problem is non-linear and is solved by an iterative  $L_1$  norm minimization technique (Wéber, 2009). To allow only forward slip during the rupture process, we impose a positivity constraint on the STF. After the decomposition of the MTRFs, a large number of moment tensor and STF solutions are obtained that can be considered as samples from their respective PPDFs.

Summing up, the applied non-linear waveform inversion approach maps the PPDFs for the hypocentral coordinates, the moment tensor, and the STF. In this study we generated 1000 samples according to the *a posteriori* distributions. The final estimates for the focal parameters are given

by the maximum likelihood points.

Šílený *et al.* (1992) and, more recently, Vavryčuk and Kühn (2012) also describe seismic point sources by six independent MTRFs and invert waveforms for moment tensor and STF in two steps. Šílený *et al.* (1992) work in the time domain, whereas Vavryčuk and Kühn (2012) calculate the MTRFs and STF in the frequency domain and estimate the moment tensor in the time domain. The main difference between these methods and our waveform inversion procedure used in this study is that our approach is a fully non-linear probabilistic one in both the hypocenter (centroid) determination and the moment tensor estimation.

In order to analyze the distribution of the retrieved moment tensors, we first deduce their principal axes. Then each moment tensor is decomposed into an isotropic (ISO) part, representing an explosive or implosive component, and into a deviatoric part, containing both the double-couple (DC) and the compensated linear vector dipole (CLVD) components (Jost and Herrmann, 1989). Finally, the 900 mechanisms (90 per cent of the 1000 Monte Carlo solutions) yielding the best goodness of fit values are displayed on the focal sphere as a scatter plot. The extent of this scatter plot approximates well the 90 per cent confidence region for the moment tensor.

In this study, the method of Riedesel and Jordan (1989) is employed to display the scatter plot of the moment tensor solution. The principal vectors ( $\mathbf{e}_1, \mathbf{e}_2, \mathbf{e}_3$ ) of a moment tensor define the tension (T), neutral (N), and compression (P) axes, while the principal values ( $\lambda_1, \lambda_2, \lambda_3$ ) give their magnitudes. In the principal axis system, various unit vectors can be constructed using various linear combinations of the principal vectors. The vector that describes a general source mechanism is  $\mathbf{m} \propto \lambda_1 \mathbf{e}_1 + \lambda_2 \mathbf{e}_2 + \lambda_3 \mathbf{e}_3$ , a double-couple source mechanism has the vector representation  $\mathbf{d} \propto \mathbf{e}_1 - \mathbf{e}_3$ , the vector corresponding to a purely isotropic source is the vector  $\mathbf{i} \propto \mathbf{e}_1 + \mathbf{e}_2 + \mathbf{e}_3$ , and two possible CLVD vectors,  $\mathbf{l}_1 \propto \mathbf{e}_1 - 0.5\mathbf{e}_2 - 0.5\mathbf{e}_3$  and  $\mathbf{l}_2 \propto 0.5\mathbf{e}_1 + 0.5\mathbf{e}_2 - \mathbf{e}_3$ , can also be defined. The scatter plot for the  $\mathbf{m}$  vector, together with the  $\mathbf{d}$ ,  $\mathbf{i}$ , and  $\mathbf{l}_{1,2}$  vectors corresponding to the best moment tensor solution are then plotted on the surface of the focal sphere. The great circle that connects the  $\mathbf{d}$  and  $\mathbf{l}_{1,2}$  vectors on the unit sphere defines the subspace on which  $\mathbf{m}$  must lie for a deviatoric source. The distribution of the scatter plot of  $\mathbf{m}$  with respect to the  $\mathbf{d}$ ,  $\mathbf{i}$ , and  $\mathbf{l}_{1,2}$  vectors informs us on the statistical significance of the DC, ISO, and CLVD components of the solution: if the vector  $\mathbf{d}$  lies within the scatter plot of  $\mathbf{m}$ , the mechanism is a double-couple; for a reliable CLVD solution, the scatter plot lies on top of one of the  $\mathbf{l}_{1,2}$  vectors; and when the scatter plot lies off the deviatoric

great circle, the isotropic portion is reliable.

According to the definitions given in Bowers and Hudson (1999), the scalar seismic moments of the isotropic and deviatoric components of a general moment tensor  $\mathbf{M}$  can be determined as

$$M_{ISO} = \frac{1}{3} \cdot |\text{Tr}(\mathbf{M})| \quad (12)$$

$$M_{DEV} = \max(|\lambda_i^*|; i = 1, 2, 3) \quad (13)$$

where  $\text{Tr}(\mathbf{M}) = \lambda_1 + \lambda_2 + \lambda_3$  denotes the trace of the moment tensor  $\mathbf{M}$  and  $\lambda_i^* = \lambda_i - \text{Tr}(\mathbf{M})/3$ . Then, to assess the relative amounts of the DC, CLVD and ISO components in a moment tensor, we calculate their percentages in the following way:

$$ISO = \frac{M_{ISO}}{M_{ISO} + M_{DEV}} \times 100 \quad (\%) \quad (14)$$

$$CLVD = 2 \frac{|\lambda_{|\min|}^*|}{|\lambda_{|\max|}^*|} \times (100 - ISO) \quad (\%) \quad (15)$$

$$DC = 100 - ISO - CLVD \quad (\%) \quad (16)$$

where subscripts  $|\min|$  and  $|\max|$  refer to the minimum and the maximum of the absolute values of  $\lambda_i^*$ . Equations (14)–(16) follow the definitions in the MoPaD tool (Krieger and Heimann, 2012) and slightly differ from those given in Vavryčuk (2005). The ISO and CLVD components are called the non-DC components of  $\mathbf{M}$ . Due to errors and incompatibilities in the observed seismograms, as well as the incomplete knowledge of the velocity distribution and earthquake hypocenter, waveform inversion always produces earthquake mechanisms with non-DC components.

## Mainshock

For estimating the full moment tensor of the Oroszlány mainshock, we used seismograms recorded at nine local seismic stations. The stations and components were manually selected based on the signal-to-noise ratio. Unfortunately, at two short-period PMMN stations near the epicenter (PKSG and PKST), the large-amplitude S-waves were clipped by the acquisition system and thus not used in the inversion. A causal bandpass filter from 0.5 to 2 Hz was applied to the waveforms after transforming them to displacement. The same filter was applied to the displacement Green's functions. The

value of the lower cut-off frequency was dictated by the natural frequencies of the short-period stations. Because short wavelengths are more affected by small-scale heterogeneities of the medium not modeled in our simple 1D velocity model, the high-frequency content of the waveforms to be inverted should be kept at a minimum. After some experience we found that below 2 Hz our inversion method produced stable solutions.

Our simple 1D earth model allows us to model sufficiently the beginning of the P and S wave-trains, but it is not detailed enough to model reflected/converted waves. For this reason, in the inversion procedure we used first-arrival body waves only. For the vertical and radial components, the processed time window started at the arrival of the P-phase, whereas for the transverse component it started at the S-phase. The length of the time window was chosen according to the epicentral distance but it was shortened for some stations when it became evident that the latter part of the seismograms had not been recovered satisfactorily. The synthetic waveforms (GFs) were windowed in the same way as the observed ones. Because differences between the true earth structure and our 1D model considerably affect the arrival time of seismic phases, before performing the waveform inversion we applied a time shift between the synthetics and the data to obtain the optimal correlation between them. We allowed different time shifts for the P-phase and the S-phase.

The waveform inversion results for the mainshock are presented in Fig. 6 and Table 4 (Event #1). The retrieved optimum centroid is about 1.5 km to south-southeast from the epicenter at a depth of 9 km. Fig. 7 compares the observed seismograms and synthetic waveforms computed using the best (maximum likelihood) source parameters. Due to the good signal-to-noise ratio and the azimuthally well-distributed recording stations, the waveforms are fitted fairly well.

The retrieved mechanism is in agreement with the available clear readings of first-arrival P-wave polarities and shows strike-slip faulting (Fig. 6). Fault slip is either right-lateral on a north–south-striking, or left-lateral on an east–west-striking nodal plane. The DC component of the moment tensor is 84 per cent. The STF has a single peak significant at the 90 per cent confidence level. The MT scatter plot contains the DC vector suggesting that the non-DC components have no statistical significance and a pure DC can be considered as the solution of the inversion. The confined zones of the principal axes allow only a small variation of the orientation of the mechanism.

In order to investigate the robustness of our moment tensor solution, we repeated the whole inversion procedure using only the six seismic stations with the smallest epicentral distances. The

obtained results are shown in Table 4 and Fig. 6. The retrieved centroid coordinates agree with the previous ones and the source mechanism did not change significantly as well. The uncertainty of the principal axes increased a little bit, but it does not influence the reliability of the resulting mechanism. These results show that our solution can be considered as robust.

In the on-line catalogs of the USGS NEIC, the GFZ German Research Centre for Geosciences, and the Istituto Nazionale di Geofisica e Vulcanologia (INGV), regional moment tensor solutions are published for the Oroszlány main event. These regional moment tensors show very good agreement with the source mechanisms retrieved in this basically local study (Fig. 8, Table 4). The USGS NEIC solution is a pure DC mechanism, whereas the other two are pure deviatoric ones with high CLVD percentages. With respect to the centroid depth, our estimation of 9 km is smaller than those obtained by the three agencies. The moment magnitude  $M_w = 4.0$  of our solution is also slightly lower than those from the other solutions ( $M_w = 4.2 - 4.4$ ). Nevertheless, we can conclude that the waveform inversion method applied in this study is suitable to estimate the earthquake source mechanism with sufficient reliability using local waveforms exclusively.

## Aftershocks

The Oroszlány mainshock was followed by four aftershocks with local magnitude varying between 2.0 and 2.7. They were recorded by at least five seismic stations with signal-to-noise ratio large enough to estimate their moment tensors using our waveform inversion procedure. To remove the low- and high-frequency noise from the relatively low-magnitude seismograms, we applied a causal bandpass filter from 1.0 to 2.5 Hz to the displacement waveforms. The obtained source mechanisms are illustrated in Fig. 6 and listed in Table 4.

Three of the analyzed aftershocks have strike-slip mechanism very similar to that of the mainshock, whereas the moment tensor of the fourth one (Event #28) shows thrust faulting with some strike-slip component. All the retrieved mechanisms are in agreement with the first-arrival P-wave polarities and the percentage of the DC component varies between 81 and 89 per cent. The STFs have a single peak significant at the 90 per cent confidence level. According to the MT scatter plots, the non-DC components of the solutions are statistically insignificant. The scatter plots of the principal axes show that the orientation of the mechanisms are well resolved. The sub-horizontal P-axis strikes about north-east–south-west for both the mainshock and all the analyzed aftershocks,

coinciding with the general trend of the compressional stress field in the epicentral region (Bada *et al.*, 1999; Gerner *et al.*, 1999). In Fig. 9 we summarize our source mechanism solutions on a map of the source area.

## Summary

In this paper we analyzed all seismic data available to us for the Oroszlány mainshock and its 67 aftershocks in order to estimate their source parameters. Using a number of techniques we were able to demonstrate that the main source properties can be determined with acceptable uncertainties for relatively small earthquakes in north-west Hungary.

According to the inversion of arrival times, the epicentral coordinates of the mainshock were  $18.375^\circ\text{E} \pm 0.8 \text{ km}$  and  $47.482^\circ\text{N} \pm 1.4 \text{ km}$  (90 per cent confidence) with an origin time of 17:41:38 UTC. The selected 67 aftershocks were confined to a small region of a few squared kilometers next to the mainshock. Considering the size of the epicentral error ellipses, we can safely conclude that the earthquakes studied in this paper occurred practically in a single small-scale seismogenic zone. The hypocentral depth of the main event was  $5.1 \pm 1.6 \text{ km}$ . Most of the aftershocks occurred in the depth region of 6–8 km.

We have determined the moment magnitude of the mainshock in two different ways giving an  $M_w = 4.0$  from waveform inversion and an  $M_w = 4.2$  from spectral analysis. The mismatch of the two estimates is not significant. The moment magnitudes of the spectrally analyzed aftershocks varies between 1.5 and 2.7.

Spectral source parameters were determined from displacement source spectra. The retrieved parameters agree well with the results of Süle and Wéber (2013). The estimated source radius is about 1 km for the mainshock and varies between 62 and 335 m for the aftershocks. The derived static stress drop spans from  $0.44 \times 10^5$  to  $17.60 \times 10^5 \text{ Pa}$ . All but one estimated stress drop values are less than 1 MPa, significantly smaller than the value of 10 MPa suggested by Kanamori and Anderson (1975) for intraplate earthquakes. This observation may be attributed to the general weakness of the lithosphere due to the updoming of the mantle and the strong geothermal anomaly characteristic to the inner part of the Pannonian basin.

We have successfully estimated the full moment tensor of the mainshock and its four aftershocks ( $2.0 \leq M_L \leq 2.7$ ) using a local waveform inversion procedure. The non-DC components of the solu-

tions are statistically insignificant. The negligible amount of the ISO component implies the tectonic nature of the investigated events. In general, the obtained centroids differ from the hypocenters just within the calculated location errors.

The moment tensor computed for the mainshock shows a strike-slip mechanism with either right-lateral slip on a north–south-striking, or left-lateral movement on an east–west-striking nodal plane. Our result shows very good agreement with the regional moment tensor solutions published by other agencies. Three of the analyzed aftershocks also had strike-slip mechanisms very similar to that of the mainshock, whereas one event was a thrust faulting earthquake with some strike-slip component. The sub-horizontal P-axis struck about north-east–south-west for both the mainshock and all the analyzed aftershocks, agreeing well with the main stress pattern published for the source area.

## Data and resources

Seismograms recorded by the Hungarian National Seismological Network are available upon request. Waveforms from the Paks Microseismic Monitoring Network were provided by Georisk Ltd.; these data are not accessible to the public. Earthquake locations and regional moment tensor solutions were taken from public catalogs of the ISC (<http://www.isc.ac.uk>, last accessed May 2013), USGS NEIC (<http://earthquake.usgs.gov/earthquakes/>, last accessed May 2013), GFZ (<http://geofon.gfz-potsdam.de>, last accessed May 2013), EMSC (<http://www.emsc-csem.org>, last accessed May 2013), and INGV (<http://www.bo.ingv.it/RCMT/>, last accessed May 2013).

The synthetic Green’s functions were computed using the computer program `hspec96`, version 3.3, developed by Robert Herrmann, Department of Earth and Atmospheric Sciences, Saint Louis University. This program is contained in Computer Programs in Seismology, a software package available at <http://www.eas.slu.edu/People/RBHerrmann/CPS330.html> (last accessed May 2013). Earthquake locations were estimated using the NonLinLoc software package developed by Anthony Lomax (<http://alomax.free.fr/software.html>, last accessed May 2013). Figures were prepared using the Generic Mapping Tools software, version 4.5.8 (Wessel and Smith, 1998).



## Acknowledgments

The reported investigation was financially supported by the TAMOP-4.2.2.C-11/1/KONV-2012-0015 (Earth-system) project sponsored by the EU and European Social Foundation. We thank J. Zahradnik and an anonymous reviewer for making various suggestions, which have helped us in improving this paper. We are also grateful to Georisk Ltd. for providing the waveform data recorded by the Paks Microseismic Monitoring Network.

## References

- Archuleta, R. J., E. Cranswick, C. Mueller, and P. Spudich (1982). Source parameters of the 1980 Mammoth Lakes, California, earthquake sequence, *J. Geophys. Res.* **87**, 4595–4607.
- Bada, G., F. Horváth, P. Gerner, and I. Fejes (1999). Review of the present-day geodynamics of the Pannonian basin: progress and problems, *J. Geodynamics* **27**, 501–527.
- Bakun, W. H., and W. Joyner (1984). The  $M_L$  scale in Central California, *Bull. Seismol. Soc. Am.* **74**, 1827–1843.
- Bowers, D., and J. A. Hudson (1999). Defining the scalar moment of a seismic source with a general moment tensor, *Bull. Seismol. Soc. Am.* **89**, 1390–1394.
- Brune, J. N. (1970). Tectonic stress and the spectra of seismic shear waves from earthquakes, *J. Geophys. Res.* **75**, 4997–5009.
- Fodor, L., G. Bada, G. Csillag, E. Horváth, Zs. Ruszkiczay-Rüdiger, K. Palotás, F. Síkhegyi, G. Timár, S. Cloetingh, and F. Horváth (2005). An outline of neotectonic structures and morphotectonics of the western and central Pannonian basin, *Tectonophysics* **410**, 15–41.
- Font, Y., H. Kao, S. Lallemand, C.-S. Liu, and L.-Y. Chiao (2004). Hypocentre determination offshore of eastern Taiwan using the Maximum Intersection method, *Geophys. J. Int.* **158**, 655–675., doi: 10.1111/j.1365-246X.2004.02317.x
- Gerner, P., G. Bada, P. Dövényi, B. Müller, M. C. Oncescu, S. Cloetingh, and F. Horváth (1999). Recent tectonic stress and crustal deformation in and around the Pannonian Basin: data and models, in *The Mediterranean Basins: Tertiary Extension within the Alpine Orogen*, B. Durand,

- L. Jolivet, F. Horváth, and M. Seranne (Editors), Geological Society, London, Special Publications **156**, 269–294.
- Gráczér, Z., and Z. Wéber (2012). One-dimensional P-wave velocity model for the territory of Hungary from local earthquake data, *Acta Geod. Geoph. Hung.* **47**, 344–357., doi: 10.1556/AGeod.47.2012.3.5
- Gráczér, Z., T. Czifra, M. Kiszely, P. Mónus, and T. Zsíros (2012). *Hungarian National Seismological Bulletin 2011*, Kövesligethy Radó Seismological Observatory, MTA CSFK GGI, Budapest.
- Grenerczy, Gy., A. Kenyeres, and I. Fejes (2000). Present crustal movement and strain distribution in central Europe inferred from GPS measurements, *J. Geophys. Res.* **105**, 21835–21846.
- Grenerczy, Gy., G. Sella, S. Stein, and A. Kenyeres (2005). Tectonic implications of the GPS velocity field in the northern Adriatic region, *Geophys. Res. Lett.* **32**, L16311, doi: 10.1029/2005GL022947
- Hanks, T.C., and H. Kanamori (1979). A moment-magnitude scale, *J. Geophys. Res.* **84**, 2348–2350.
- Hanks, T.C., and M. Wyss (1972). The use of body-wave spectra in the determination of seismic-source parameters, *Bull. Seismol. Soc. Am.* **62**, 561–589.
- Havskov, J., and L. Ottemöller (2010). *Routine Data Processing in Earthquake Seismology*, Springer, Dordrecht Heidelberg London New York
- Havskov, J., J. A. Peña, J. M. Ibáñez, L. Ottemöller, and C. Martínez-Arévalo (2003). Magnitude scales for very local earthquakes. Application for Deception Island Volcano (Antarctica), *J. Volcanol. Geotherm. Res.* **128**, 115–133.
- Herrmann, R.B., and C. Y. Wang (1985). A comparison of synthetic seismograms, *Bull. Seismol. Soc. Am.* **75**, 41–56.
- Jost, M. L., and R. B. Herrmann (1989). A student’s guide to and review of moment tensors, *Seism. Res. Lett.* **60**, 37–57.
- Kanamori, H., and D. L. Anderson (1975). Theoretical basis of some empirical relations in seismology, *Bull. Seismol. Soc. Am.* **65**, 1073–1095.

- Krieger, L., and S. Heimann (2012). MoPaD: Moment tensor plotting and decomposition: A tool for graphical and numerical analysis of seismic moment tensors, *Seism. Res. Lett.* **83**, 589–595.
- Lomax, A., and A. Curtis (2001). Fast, probabilistic earthquake location in 3D models using oct-tree importance sampling, *Geophys. Res. Abstr.* **3**, 955.
- Lomax, A., J. Virieux, P. Volant, and C. Thierry-Berge (2000). Probabilistic earthquake location in 3D and layered models: Introduction of a Metropolis-Gibbs method and comparison with linear locations, in *Advances in Seismic Event Location*, C. H. Thurber, and N. Rabinowitz (Editors), Kluwer, Amsterdam, 101–134,
- Riedesel, M. A., and T. H. Jordan (1989). Display and assessment of seismic moment tensors, *Bull. Seismol. Soc. Am.* **79**, 85–100.
- Rubinstein, R.Y., and D. P. Kroese (2008). *Simulation and the Monte Carlo Method*, John Wiley & Sons, Hoboken, New Jersey.
- Šílený, J., G. F. Panza, and P. Campus (1992). Waveform inversion for point source moment tensor retrieval with variable hypocentral depth and structural model, *Geophys. J. Int.* **109**, 259–274.
- Singh, S. K., R. J. Apsel, J. Fried, and J. N. Brune (1982). Spectral attenuation of SH waves along the imperial fault, *Bull. Seismol. Soc. Am.* **72**, 2003–2016.
- Süle, B., and Z. Wéber (2013). Earthquake source parameters and scaling relationships in Hungary (central Pannonian basin), *J. Seismology* **17**, 507-521., doi: 10.1007/s10950-012-9334-3
- Tóth, L., P. Mónus, T. Zsiros, and M. Kiszely (2002). Seismicity in the Pannonian Region - earthquake data, *EGU Stephan Mueller Special Publication Series* **3**, 9–28.
- Vavryčuk, V. (2005). Focal mechanisms in anisotropic media, *Geophys. J. Int.* **161**, 334–346.
- Vavryčuk, V., and D. Kühn (2012). Moment tensor inversion of waveforms: a two-step time-frequency approach, *Geophys. J. Int.* **190**, 1761–1776.
- Wang, C. Y., and R. B. Herrmann (1980). A numerical study of P-, SV-, and SH-wave generation in a plane layered medium, *Bull. Seismol. Soc. Am.* **70**, 1015–1036.

- Wéber, Z. (2006). Probabilistic local waveform inversion for moment tensor and hypocentral location, *Geophys. J. Int.* **165**, 607–621., doi: 10.1111/j.1365-246X.2006.02934.x
- Wéber, Z. (2009). Estimating source time function and moment tensor from moment tensor rate functions by constrained L1 norm minimization, *Geophys. J. Int.* **178**, 889–900., doi: 10.1111/j.1365-246X.2009.04202.x
- Wessel, P., and W. H. F. Smith (1998). New, improved version of Generic Mapping Tools released, *EOS Trans. AGU* **79**, 579.
- Zsíros, T. (2000). *Seismicity and seismic hazard in the Carpathian Basin: Hungarian earthquake catalog (456–1995)* (in Hungarian), MTA FKK GGKI, Budapest

## **Authors' affiliations, addresses**

Kövesligethy Radó Seismological Observatory  
Geodetic and Geophysical Institute  
Research Centre for Astronomy and Earth Sciences  
Hungarian Academy of Sciences  
Meredek utca 18.  
H-1112 Budapest, Hungary  
weber@seismology.hu (Z.W.); suba@seismology.hu (B.S.)

Table 1: The 1D earth model used in this study.

Layer thickness (km)	P-wave velocity (km/s)	S-wave velocity (km/s)	Density (g/cm <sup>3</sup> )
3.0	5.30	3.05	2.76
16.0	5.74	3.30	2.85
7.0	6.29	3.61	2.96
∞	7.93	4.56	3.29

P- and S-wave velocities are after Gráczér and Wéber (2012). For density  $\rho$ , an empirical law is used:  $\rho = 1.7 + 0.2v_P$ , where  $\rho$  is measured in g/cm<sup>3</sup> and  $v_P$  in km/s.

Table 2: Estimated hypocentral parameters of the studied earthquakes.

Event No.	Date (yyyy-mm-dd)	Time (hh:mm:ss)	Lon. (°E)	Lat. (°N)	Depth (km)	Covariance (km <sup>2</sup> )						$M_L$
						$C_{xx}$	$C_{xy}$	$C_{xz}$	$C_{yy}$	$C_{yz}$	$C_{zz}$	
1	2011-01-29	17:41:38	18.375	47.482	5.1	0.233	-0.083	0.078	0.690	-0.540	0.927	4.5
2	2011-01-29	17:44:43	18.367	47.471	7.6	0.636	0.041	-0.029	3.923	-2.353	4.685	1.5
3	2011-01-29	17:46:49	18.353	47.479	8.5	1.457	-0.874	1.523	7.303	-4.175	9.227	0.7
4	2011-01-29	17:56:36	18.363	47.463	7.2	0.633	-0.208	0.427	4.095	-2.205	4.437	0.3
5	2011-01-29	18:05:31	18.373	47.471	8.0	0.428	-0.048	0.003	3.087	-1.716	4.064	1.6
6	2011-01-29	18:18:34	18.357	47.470	5.5	0.367	-0.171	-0.023	2.533	-1.413	2.777	1.7
7	2011-01-29	19:40:02	18.365	47.466	7.4	0.574	-0.174	0.107	3.886	-1.618	5.119	1.0
8	2011-01-29	19:57:54	18.362	47.461	7.6	0.986	-0.176	0.460	5.519	-2.953	5.162	0.5
9	2011-01-29	20:42:20	18.371	47.465	7.6	0.786	0.201	0.026	5.090	-2.056	4.505	0.5
10	2011-01-29	20:51:07	18.375	47.468	6.9	0.525	-0.094	0.097	3.628	-1.962	4.261	1.3
11	2011-01-29	20:52:47	18.364	47.468	7.0	0.614	-0.091	0.244	3.687	-2.014	4.474	0.9
12	2011-01-29	21:06:27	18.367	47.475	6.3	0.717	-0.175	0.192	4.168	-2.221	5.226	0.7
13	2011-01-29	23:02:05	18.354	47.466	6.1	0.650	0.187	0.093	3.472	-1.564	4.549	0.3
14	2011-01-29	23:36:49	18.363	47.468	7.2	0.661	0.016	0.274	3.963	-2.207	4.545	0.4
15	2011-01-29	23:50:30	18.368	47.466	6.9	0.608	-0.174	0.247	4.031	-2.030	4.449	0.4
16	2011-01-30	00:19:11	18.365	47.468	7.8	0.404	-0.252	0.198	2.673	-1.913	4.424	1.4
17	2011-01-30	00:31:08	18.367	47.471	7.5	0.528	0.257	-0.078	4.422	-2.588	5.112	1.1
18	2011-01-30	01:27:50	18.366	47.461	7.0	0.585	0.142	0.167	3.970	-1.699	4.369	0.4
19	2011-01-30	01:35:13	18.365	47.469	7.4	0.549	0.023	0.230	3.889	-2.015	4.361	0.6
20	2011-01-30	04:41:19	18.356	47.466	6.4	0.636	-0.137	0.209	3.739	-1.827	4.173	0.7
21	2011-01-30	10:34:25	18.365	47.471	7.2	0.563	-0.280	0.396	4.265	-2.741	5.123	1.0
22	2011-01-30	13:34:29	18.367	47.480	2.8	0.488	-0.248	0.043	2.044	-0.816	2.185	2.0
23	2011-01-30	14:47:24	18.366	47.467	6.3	0.740	-0.045	0.348	4.633	-1.944	5.169	0.5
24	2011-01-30	20:58:46	18.363	47.471	5.4	0.279	-0.238	0.276	1.298	-1.370	2.179	2.7
25	2011-01-30	21:11:39	18.359	47.462	7.2	0.695	-0.341	0.406	4.388	-2.277	4.654	0.7
26	2011-01-30	21:21:34	18.365	47.466	6.9	0.691	-0.142	0.596	3.730	-2.037	5.078	0.3
27	2011-01-30	21:57:39	18.373	47.465	7.1	0.613	0.047	0.198	3.759	-1.890	4.273	0.7
28	2011-01-31	00:25:29	18.365	47.469	5.2	0.275	-0.202	0.181	1.320	-1.351	2.049	2.4
29	2011-01-31	10:05:39	18.356	47.465	6.3	0.671	-0.114	0.316	3.485	-1.925	4.406	1.2
30	2011-02-01	00:45:40	18.374	47.470	7.7	1.181	-0.836	0.176	8.363	-2.747	6.555	0.3
31	2011-02-01	02:02:45	18.363	47.462	7.3	0.555	-0.128	0.348	3.837	-2.247	4.640	0.4
32	2011-02-01	17:44:39	18.375	47.471	7.1	1.124	-0.128	0.558	0.859	0.854	3.370	0.2
33	2011-02-02	00:27:52	18.363	47.471	6.5	0.809	-0.015	0.441	0.839	1.018	3.497	0.2
34	2011-02-02	01:46:10	18.366	47.470	7.7	0.501	-0.034	0.114	0.562	0.431	1.884	0.6

Table 2: – *continued*

Event No.	Date (yyyy-mm-dd)	Time (hh:mm:ss)	Lon. (°E)	Lat. (°N)	Depth (km)	Covariance (km <sup>2</sup> )						$M_L$
						$C_{xx}$	$C_{xy}$	$C_{xz}$	$C_{yy}$	$C_{yz}$	$C_{zz}$	
35	2011-02-02	02:04:56	18.361	47.465	6.4	0.601	-0.009	0.371	0.489	0.675	2.987	0.5
36	2011-02-02	03:30:04	18.369	47.468	7.2	0.324	-0.068	-0.033	0.418	0.319	1.173	1.1
37	2011-02-02	03:54:10	18.363	47.469	6.5	1.038	-0.008	0.824	0.744	0.802	3.791	0.5
38	2011-02-02	11:29:31	18.371	47.468	7.5	0.491	-0.011	0.147	0.500	0.497	1.829	1.4
39	2011-02-04	05:37:59	18.373	47.466	6.9	1.986	-0.293	1.564	0.946	0.455	4.310	0.1
40	2011-02-04	14:23:21	18.365	47.466	7.3	0.260	0.054	0.055	0.346	0.455	1.696	1.0
41	2011-02-05	11:08:36	18.363	47.467	7.4	0.336	0.075	0.133	0.453	0.536	1.718	1.4
42	2011-02-06	12:45:24	18.375	47.468	7.3	0.406	0.075	0.089	0.477	0.529	2.061	1.1
43	2011-02-09	01:28:53	18.374	47.467	7.4	0.407	0.189	0.124	0.593	0.593	1.886	1.1
44	2011-02-09	05:44:51	18.367	47.468	7.3	1.513	0.298	0.121	1.110	1.292	3.864	0.4
45	2011-02-10	20:18:34	18.367	47.466	6.9	0.936	0.097	0.296	0.587	0.710	2.513	0.3
46	2011-02-15	01:56:29	18.375	47.466	7.3	0.836	0.175	0.703	0.598	0.747	3.008	0.4
47	2011-02-15	02:57:34	18.369	47.468	6.7	0.783	0.141	0.821	0.605	0.868	3.992	-0.1
48	2011-02-15	09:02:38	18.363	47.469	6.8	0.464	0.163	0.218	0.759	1.022	2.997	0.8
49	2011-02-16	05:15:08	18.362	47.470	6.6	0.494	0.076	0.293	0.608	0.793	2.663	0.2
50	2011-02-16	20:29:10	18.365	47.466	7.2	0.475	0.143	0.112	0.724	0.846	2.829	1.6
51	2011-02-16	21:48:41	18.375	47.469	7.5	0.362	0.065	-0.024	0.601	0.616	2.074	1.8
52	2011-02-16	22:25:03	18.375	47.469	7.8	0.468	0.135	0.098	0.676	0.727	2.216	1.6
53	2011-02-18	02:00:06	18.373	47.468	6.5	0.437	0.163	0.231	0.591	0.856	2.828	0.4
54	2011-02-18	21:43:03	18.371	47.466	6.5	0.437	0.231	0.281	0.552	0.666	2.222	0.8
55	2011-02-18	22:58:05	18.369	47.469	6.7	0.464	0.192	0.186	0.703	0.861	2.507	1.0
56	2011-02-21	01:20:21	18.371	47.469	6.6	0.794	0.121	0.734	0.891	1.163	3.784	0.7
57	2011-02-23	04:16:13	18.373	47.471	7.2	0.380	0.184	0.171	0.544	0.562	1.653	0.6
58	2011-02-23	16:50:25	18.375	47.468	7.2	0.584	0.251	0.479	0.601	0.789	2.581	1.6
59	2011-02-28	06:25:02	18.373	47.468	7.3	0.548	0.183	0.165	0.762	0.916	2.501	0.5
60	2011-02-28	07:02:44	18.373	47.466	7.1	0.389	0.140	0.125	0.476	0.570	1.933	0.8
61	2011-03-04	19:58:12	18.371	47.454	1.9	0.895	-0.328	-0.180	1.213	2.005	5.844	0.2
62	2011-03-08	13:04:32	18.361	47.466	6.0	0.485	-0.106	-0.038	0.948	1.485	4.077	0.5
63	2011-03-10	01:06:57	18.363	47.467	6.7	0.293	0.051	0.094	0.447	0.588	1.919	0.7
64	2011-03-11	01:45:24	18.365	47.467	6.6	0.225	-0.013	-0.099	0.235	0.044	0.488	2.3
65	2011-03-11	01:49:39	18.367	47.466	6.9	0.432	0.071	0.183	0.503	0.664	2.525	0.3
66	2011-03-11	15:34:54	18.363	47.465	7.1	0.444	0.049	0.213	0.521	0.635	2.447	0.9
67	2011-03-11	18:52:34	18.367	47.471	7.6	0.958	-0.001	0.543	0.620	0.665	2.843	0.1
68	2011-03-12	02:42:01	18.375	47.468	7.2	0.317	0.066	0.053	0.426	0.421	1.429	1.0

Event #1 is the 29 January 2011 Oroszlány mainshock, the rest of the events are its aftershocks. Local magnitude ( $M_L$ ) data are collected from the Hungarian National Seismological Bulletin (Gráczner *et al.*, 2012).

Table 3: Estimated spectral source parameters of the mainshock and 24 aftershocks.

Event No.	$M_L$	$M_w$	$M_0^P$ (Nm)	$EM_0^P$	$M_0^S$ (Nm)	$EM_0^S$	$f_c^P$ (Hz)	$Ef_c^P$	$f_c^S$ (Hz)	$Ef_c^S$	$r^P$ (m)	$r^S$ (m)	$\Delta\sigma^P$ ( $10^5$ Pa)	$\Delta\sigma^S$
1	4.5	4.2	1.38E+15	1.46	3.68E+15	2.16	1.9	1.39	1.3	1.73	970	972	6.67	17.60
5	1.5	1.9	3.57E+11	1.38	1.76E+12	1.70	11.7	1.03	6.6	1.59	153	185	0.44	1.21
6	1.7	2.3	5.54E+11	1.24	1.39E+13	1.53	16.0	1.37	8.1	1.78	112	221	1.70	5.56
7	1.0	1.6	2.40E+11	1.50	3.33E+11	1.20	-	-	-	-	-	-	-	-
10	1.3	1.7	2.48E+11	1.59	8.68E+11	1.68	-	-	13.8	1.88	-	88	-	5.40
16	1.4	1.7	2.10E+11	1.97	5.33E+11	2.52	-	-	-	-	-	-	-	-
17	1.1	1.6	2.81E+11	1.53	3.46E+11	2.14	-	-	-	-	-	-	-	-
21	1.0	1.6	1.47E+11	1.73	3.84E+11	2.44	-	-	-	-	-	-	-	-
22	2.0	2.2	1.94E+12	1.68	3.31E+12	2.62	10.1	1.98	7.6	1.54	176	162	1.51	3.37
24	2.7	2.7	7.68E+12	2.45	1.86E+13	3.24	5.7	1.95	5.7	1.78	318	216	1.04	8.08
28	2.4	2.5	4.91E+12	2.89	1.00E+13	2.69	5.4	1.78	5.7	1.98	335	212	0.57	8.36
29	1.2	1.7	2.53E+11	1.54	7.33E+11	1.65	-	-	-	-	-	-	-	-
36	1.1	1.6	1.88E+11	1.45	4.17E+11	1.86	-	-	-	-	-	-	-	-
38	1.4	1.9	2.38E+11	1.46	2.14E+12	1.78	-	-	-	-	-	-	-	-
40	1.0	1.6	1.68E+11	1.80	6.42E+11	1.39	-	-	-	-	-	-	-	-
41	1.4	2.0	5.79E+11	1.52	2.20E+12	2.29	-	-	-	-	-	-	-	-
42	1.1	1.8	2.91E+11	1.29	8.56E+11	1.26	-	-	-	-	-	-	-	-
43	1.1	1.5	1.34E+11	1.52	2.73E+11	1.51	-	-	-	-	-	-	-	-
50	1.6	1.6	1.40E+11	2.05	7.80E+11	1.69	-	-	9.4	1.92	-	130	-	1.53
51	1.8	2.1	9.43E+11	2.55	1.91E+12	1.97	15.8	1.29	7.5	1.93	114	162	2.80	1.93
52	1.6	2.0	7.21E+11	2.36	1.99E+12	2.55	15.6	1.50	5.1	1.55	115	240	2.07	0.63
55	1.0	1.8	4.27E+11	2.63	7.05E+11	2.07	-	-	-	-	-	-	-	-
58	1.6	1.8	2.49E+11	1.66	1.40E+12	2.18	18.4	1.33	8.7	1.81	62	140	4.44	2.21
64	2.3	2.5	3.69E+12	1.75	1.04E+13	2.48	9.8	1.78	6.0	1.93	184	204	2.52	5.38
68	1.0	1.6	1.51E+11	2.36	5.09E+11	1.71	-	-	-	-	-	-	-	-

$M_L$ : local magnitude;  $M_w$ : moment magnitude;  $M_0$ : scalar moment;  $f_c$ : corner frequency;  $r$ : source radius;  $\Delta\sigma$ : stress drop;  $EM_0$  and  $Ef_c$ : multiplicative error factor for  $M_0$  and  $f_c$ , respectively. Results are given for P- and S-wave data separately.

Table 4: Centroids and source mechanisms of the mainshock and four aftershocks.

Event No.	$M_w$	Lon. (°E)	Lat. (°N)	Depth (km)	Strike (°)	Dip (°)	Rake (°)	$DC$ (%)	$CLVD$ (%)	$ISO$ (%)	No. of stations	Source
1	4.0	18.381	47.467	9	2 / 268	76 / 73	-163 / -15	84	0	16	9	
	4.0	18.381	47.467	9	1 / 267	77 / 75	-165 / -13	86	2	12	6	
	4.2	18.320	47.560	15	355 / 265	90 / 80	-170 / 0	100	-	-	17	NEIC
	4.3	18.269	47.450	13	2 / 93	84 / 79	169 / 6	57	43	-	42	GFZ
	4.4	18.340	47.490	17	187 / 96	81 / 83	-172 / -9	63	37	-	13	INGV
22	2.0	18.372	47.458	9	354 / 85	71 / 87	177 / 19	82	1	17	6	
24	2.4	18.364	47.479	8	351 / 81	89 / 88	178 / 1	89	2	9	5	
28	2.3	18.363	47.473	8	332 / 99	51 / 54	130 / 52	81	1	18	5	
64	2.3	18.379	47.462	8	2 / 270	83 / 67	-157 / -7	82	1	17	7	

Moment magnitude ( $M_w$ ) and the number of stations used in the waveform inversion are also given. Solutions published by other agencies for the mainshock (Event #1) are indicated as well. ( $DC$ ,  $CLVD$  and  $ISO$ : percentages of the double-couple, compensated linear vector dipole and isotropic components, respectively.)

## Figure captions

Figure 1:

Map showing the most significant earthquakes that occurred in Hungary in the last 250 years (circles) and seismic stations that were operational in the country at the time of the Oroszlány event (diamonds: broad-band stations; triangles: short-period stations). Station codes and event data are also indicated. Short-period temporary stations BOKD and VSOM (inverse triangles) were operated between 1 February and 13 April, 2011, in order to better record the aftershocks. The black rectangle in the left panel encircles the seismically active Berhida - Mór - Komárom region that is enlarged in the right panel. The color version of this figure is available only in the electronic edition.

Figure 2:

*Left panel:* Epicentral solutions and their 90 per cent confidence ellipses for the 29 January 2011 Oroszlány mainshock. The depicted estimates have been determined by the present study, the EMSC, ISC, USGS NEIC, and KRSO. *Right panel:* Cross-sections of the posterior probability density function for the hypocenter of the main event illustrated as scatter density plots. Square denotes the maximum likelihood solution. Coordinates are relative to an arbitrarily chosen origin. The color version of this figure is available only in the electronic edition.

Figure 3:

Epicentral distribution of the 29 January 2011 Oroszlány mainshock and its selected 67 aftershocks as published in the Hungarian National Seismological Bulletin (left panel) and as determined in the present study (right panel). Symbol size is proportional to event magnitude. The color version of this figure is available only in the electronic edition.

Figure 4:

Plot of source radius  $r$  versus seismic moment  $M_0$  for both P- and S-waves. Solid circles represent data for the Oroszlány mainshock and its aftershocks obtained in the present study, whereas open circles depict data published in Süle and Wéber (2013). Lines of constant stress drop are also shown.  $\rho$  denotes the correlation coefficient.

Figure 5:

Relationship between local ( $M_L$ ) and moment ( $M_w$ ) magnitudes. Solid circles represent data for the Oroszlány mainshock and its aftershocks obtained in the present study, whereas open circles depict data published in Süle and Wéber (2013). The well-constrained best-fitting regression line is also



shown.  $\rho$  denotes the correlation coefficient.

Figure 6:

Source mechanisms and scatter density plots for the Oroszlány mainshock (Event #1) and its four most significant aftershocks obtained by local waveform inversion. For displaying the scatter plot of the moment tensor (MT), the method of Riedesel and Jordan (1989) is employed (solid circle:  $\mathbf{m}$  vector representing the moment tensor solution; square:  $\mathbf{d}$  vector for the DC component; triangles:  $\mathbf{l}_{1,2}$  vectors for the CLVD components; inverse triangle:  $\mathbf{i}$  vector for the isotropic part). The great circle connecting the  $\mathbf{d}$  and  $\mathbf{l}_{1,2}$  vectors defines pure deviatoric mechanisms. The 90 per cent confidence regions for the  $\mathbf{m}$  vector and the principal axes are approximated well by the extent of the corresponding scatter plots. The STF plot represents how the moment rate changes with time. The thin grey lines illustrate the 90 per cent confidence region. The beach ball represents the deviatoric part of the mechanism (shaded area: compression; open area: dilatation). First-arrival P-wave polarities are indicated as well (solid circle: compression; open circle: dilatation). Equal area projection of lower hemisphere is used. The color version of this figure is available only in the electronic edition.

Figure 7:

Waveform comparison for the Oroszlány mainshock. The observed seismograms (grey lines) are bandpass filtered with cut-off frequencies of 0.5 and 2 Hz. The synthetic waveforms (black lines) are computed using the MTRFs obtained by waveform inversion. On the left-hand side of each row, station code, epicentral distance in km (dist), and station azimuth (az) are indicated. The numbers on the right-hand side of each waveform represent the normalized correlation (corr) and the maximum amplitude in nm (amp). Waveform fit for components not used in the inversion is also shown. For station locations, see Fig. 1.

Figure 8:

Comparison of the regional moment tensor solutions for the Oroszlány mainshock obtained by the USGS NEIC, the GFZ, and the INGV with the source mechanisms estimated in this paper using waveforms recorded at 9 and 6 seismic stations, respectively. Only deviatoric components are shown (shaded area: compression; open area: dilatation). Equal area projection of lower hemisphere is used.

Figure 9:

Source mechanisms of the Oroszlány mainshock (Event #1) and its four most significant aftershocks on a map of the source area. Event numbers are also indicated. Beachball size is proportional to event magnitude (shaded area: compression; open area: dilatation). Equal area projection of lower hemisphere is used. The color version of this figure is available only in the electronic edition.

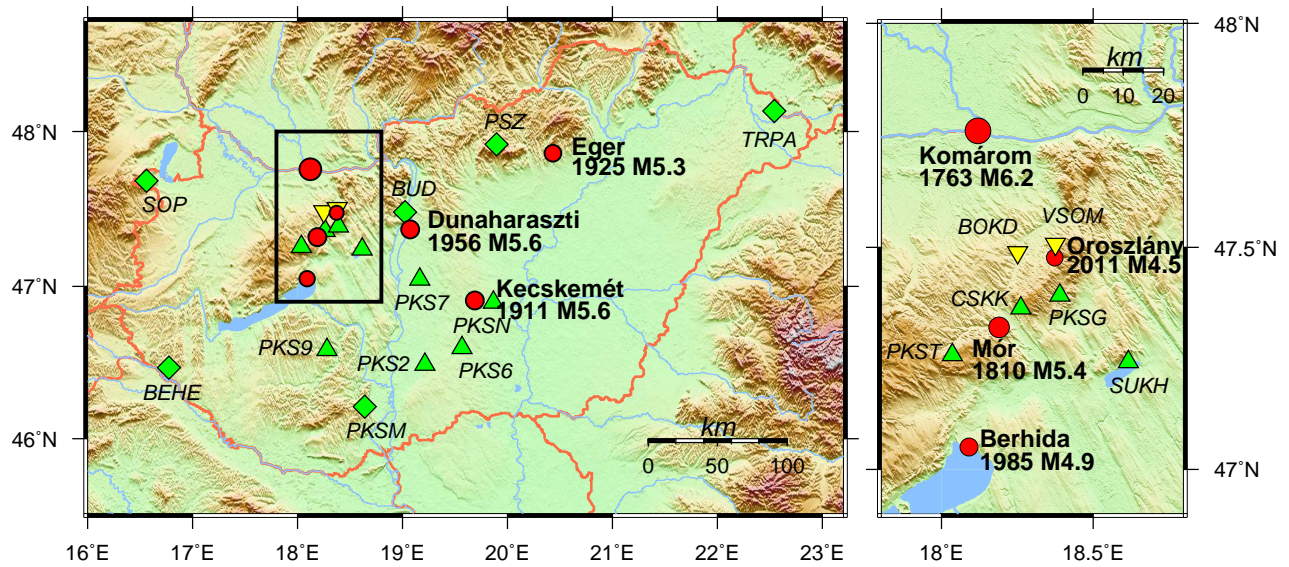


Figure 1: Map showing the most significant earthquakes that occurred in Hungary in the last 250 years (circles) and seismic stations that were operational in the country at the time of the Oroszlány event (diamonds: broad-band stations; triangles: short-period stations). Station codes and event data are also indicated. Short-period temporary stations BOKD and VSOM (inverse triangles) were operated between 1 February and 13 April, 2011, in order to better record the aftershocks. The black rectangle in the left panel encircles the seismically active Berhida - Mór - Komárom region that is enlarged in the right panel. The color version of this figure is available only in the electronic edition.

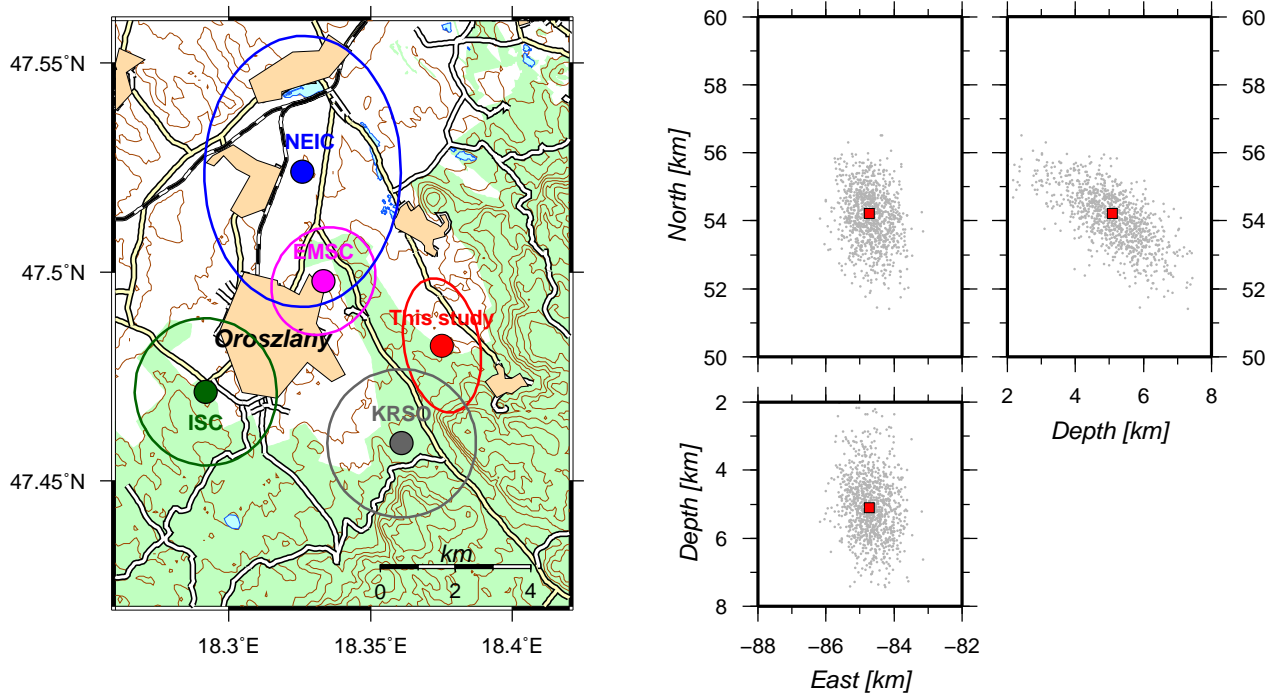


Figure 2: *Left panel:* Epicentral solutions and their 90 per cent confidence ellipses for the 29 January 2011 Oroszlány mainshock. The depicted estimates have been determined by the present study, the EMSC, ISC, USGS NEIC, and KRSO. *Right panel:* Cross-sections of the posterior probability density function for the hypocenter of the main event illustrated as scatter density plots. Square denotes the maximum likelihood solution. Coordinates are relative to an arbitrarily chosen origin. The color version of this figure is available only in the electronic edition.

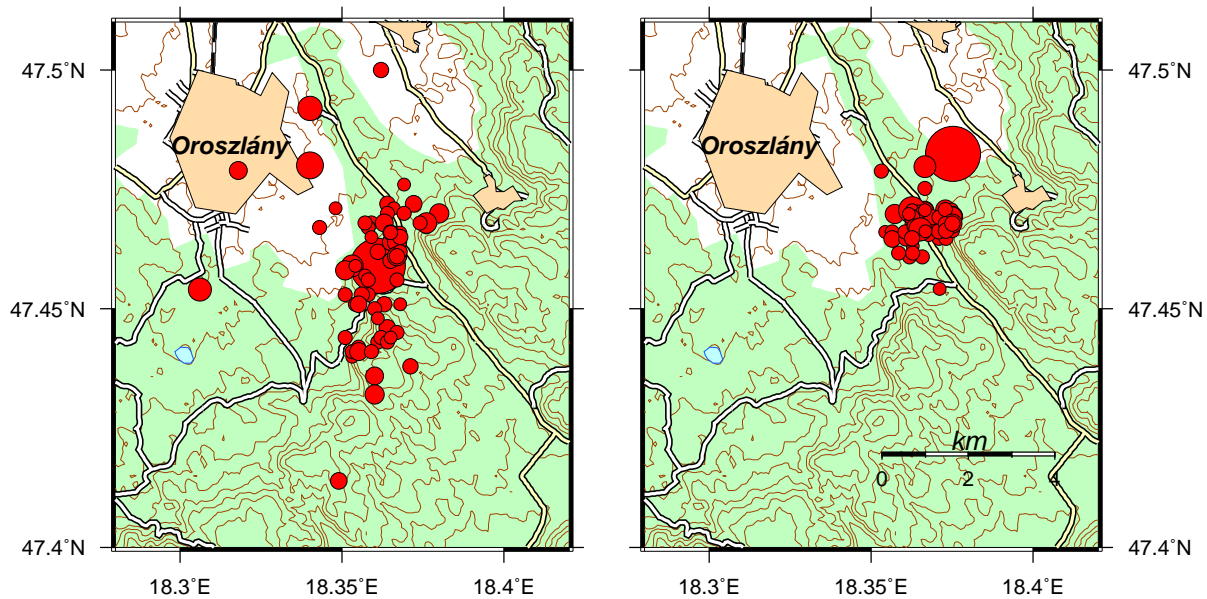


Figure 3: Epicentral distribution of the 29 January 2011 Oroszlány mainshock and its selected 67 aftershocks as published in the Hungarian National Seismological Bulletin (left panel) and as determined in the present study (right panel). Symbol size is proportional to event magnitude. The color version of this figure is available only in the electronic edition.

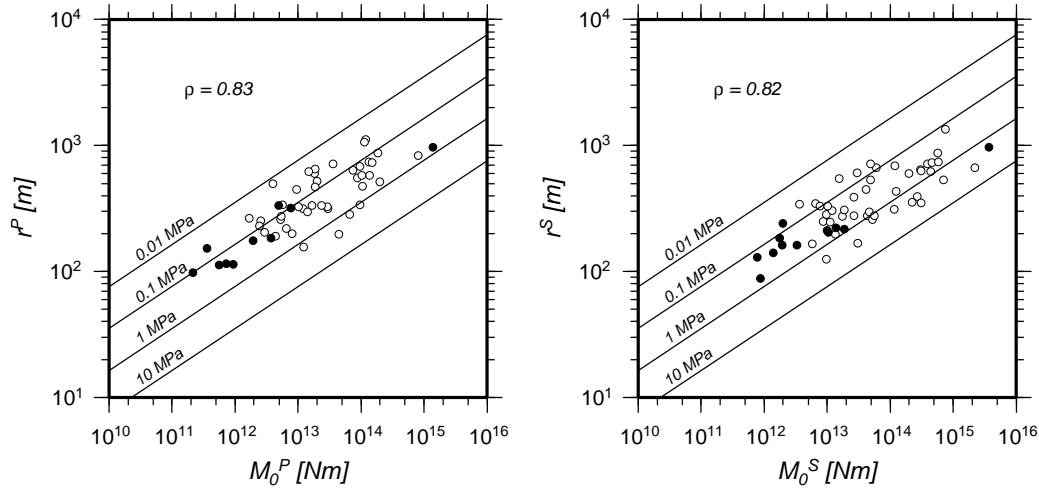


Figure 4: Plot of source radius  $r$  versus seismic moment  $M_0$  for both P- and S-waves. Solid circles represent data for the Oroszlány mainshock and its aftershocks obtained in the present study, whereas open circles depict data published in Süle and Wéber (2013). Lines of constant stress drop are also shown.  $\rho$  denotes the correlation coefficient.

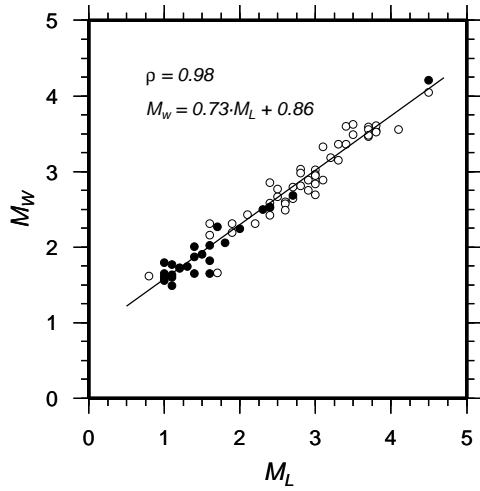


Figure 5: Relationship between local ( $M_L$ ) and moment ( $M_w$ ) magnitudes. Solid circles represent data for the Oroszlány mainshock and its aftershocks obtained in the present study, whereas open circles depict data published in Süle and Wéber (2013). The well-constrained best-fitting regression line is also shown.  $\rho$  denotes the correlation coefficient.

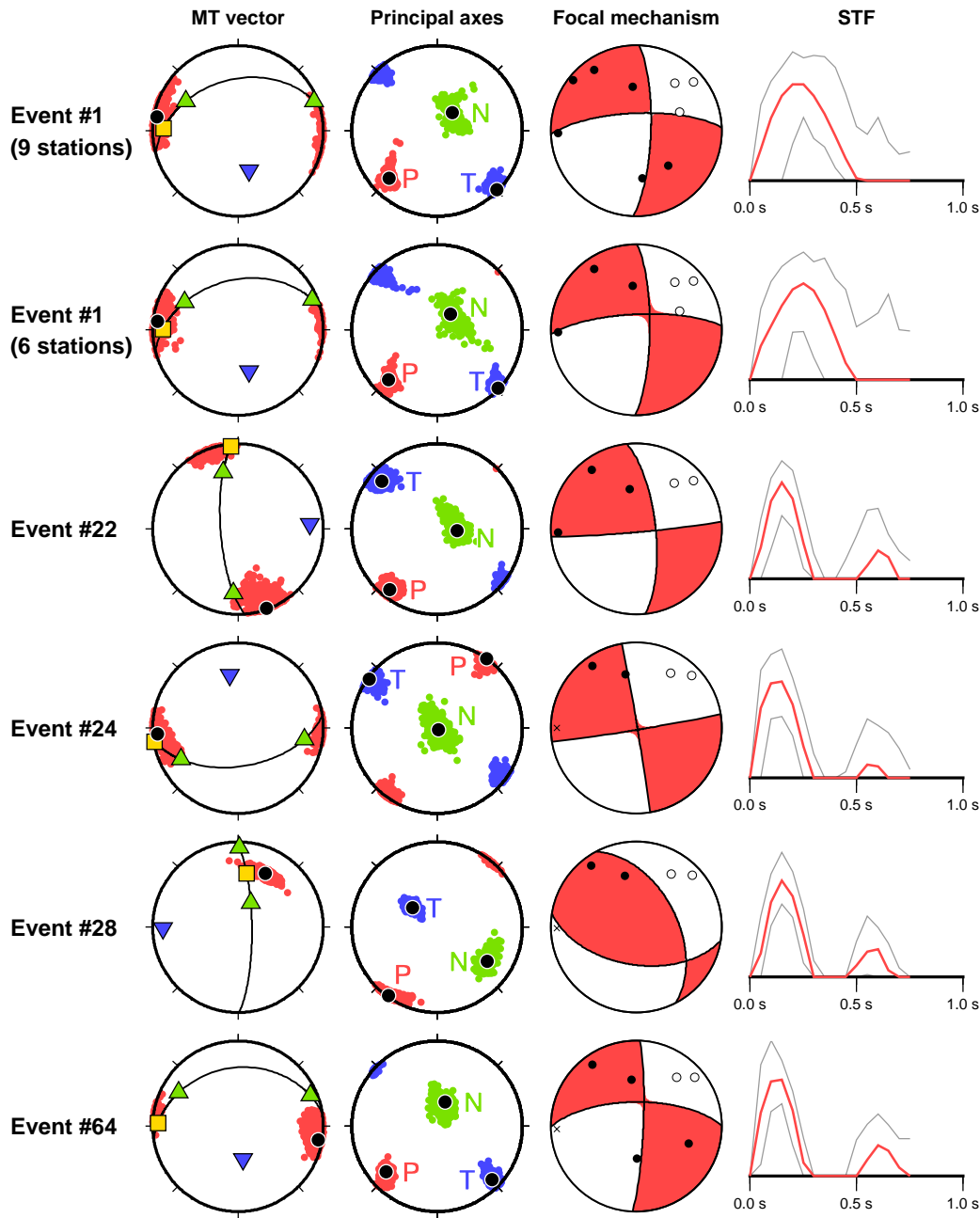


Figure 6: Source mechanisms and scatter density plots for the Oroszlány mainshock (Event #1) and its four most significant aftershocks obtained by local waveform inversion. For displaying the scatter plot of the moment tensor (MT), the method of Riedesel and Jordan (1989) is employed (solid circle:  $\mathbf{m}$  vector representing the moment tensor solution; square:  $\mathbf{d}$  vector for the DC component; triangles:  $\mathbf{l}_{1,2}$  vectors for the CLVD components; inverse triangle:  $\mathbf{i}$  vector for the isotropic part). The great circle connecting the  $\mathbf{d}$  and  $\mathbf{l}_{1,2}$  vectors defines pure deviatoric mechanisms. The 90 per cent confidence regions for the  $\mathbf{m}$  vector and the principal axes are approximated well by the extent of the corresponding scatter plots. The STF plot represents how the moment rate changes with time. The thin grey lines illustrate the 90 per cent confidence region. The beach ball represents the deviatoric part of the mechanism (shaded area: compression; open area: dilatation). First-arrival P-wave polarities are indicated as well (solid circle: compression; open circle: dilatation). Equal area projection of lower hemisphere is used. The color version of this figure is available only in the electronic edition.

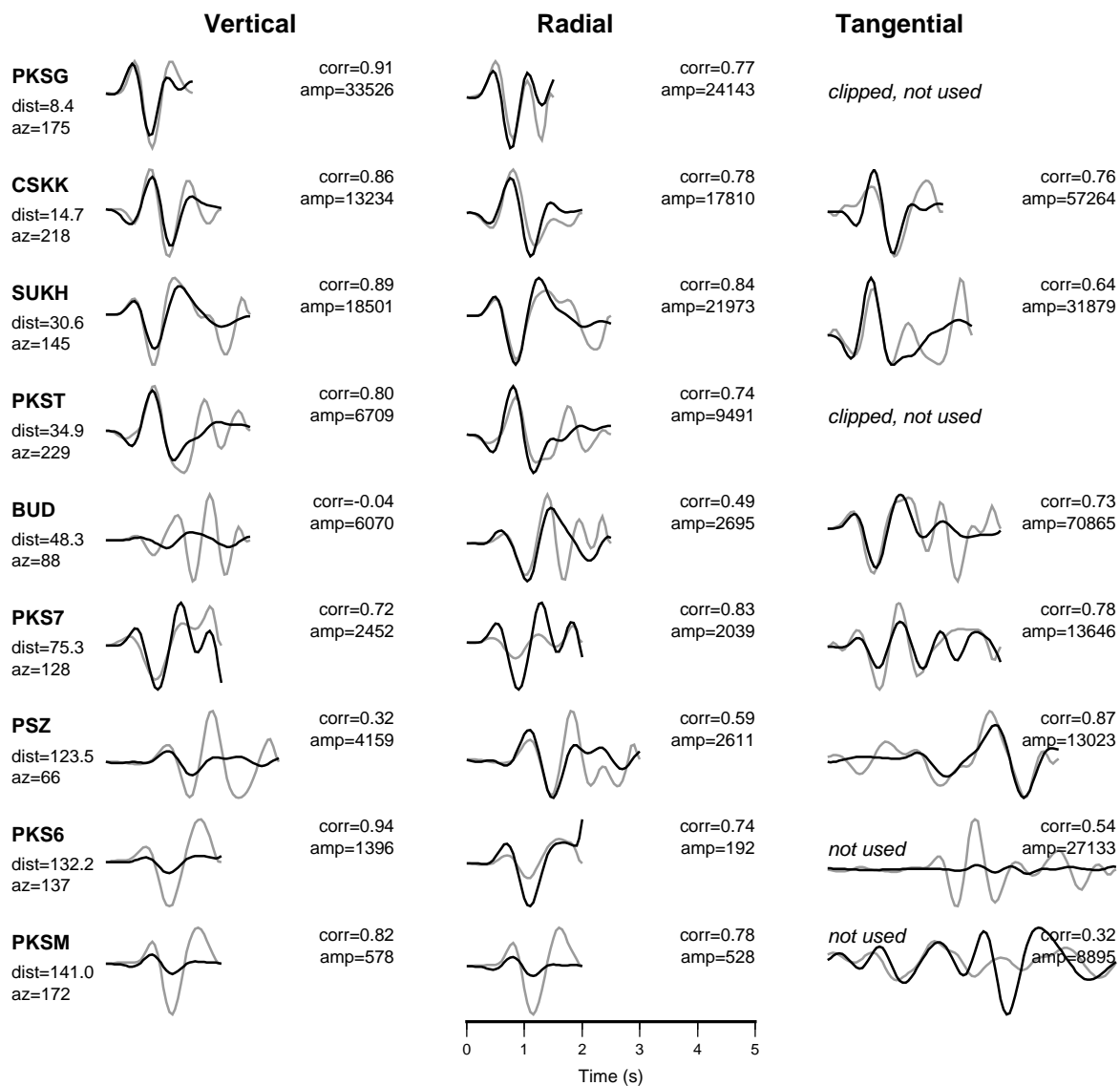


Figure 7: Waveform comparison for the Oroszlány mainshock. The observed seismograms (grey lines) are bandpass filtered with cut-off frequencies of 0.5 and 2 Hz. The synthetic waveforms (black lines) are computed using the MTRFs obtained by waveform inversion. On the left-hand side of each row, station code, epicentral distance in km (dist), and station azimuth (az) are indicated. The numbers on the right-hand side of each waveform represent the normalized correlation (corr) and the maximum amplitude in nm (amp). Waveform fit for components not used in the inversion is also shown. For station locations, see Fig. 1.

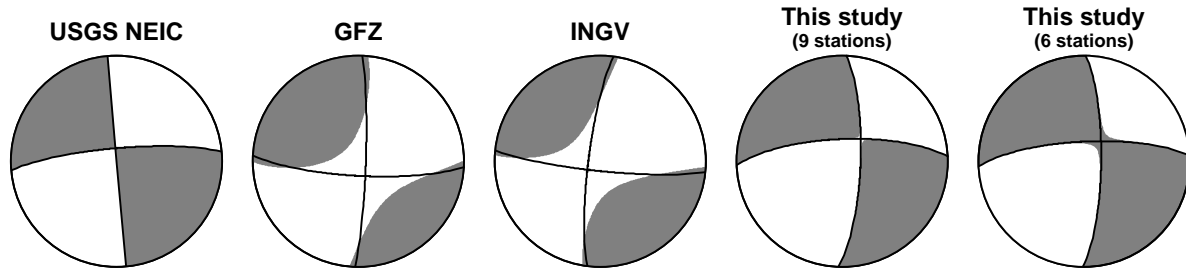


Figure 8: Comparison of the regional moment tensor solutions for the Oroszlány mainshock obtained by the USGS NEIC, the GFZ, and the INGV with the source mechanisms estimated in this paper using waveforms recorded at 9 and 6 seismic stations, respectively. Only deviatoric components are shown (shaded area: compression; open area: dilatation). Equal area projection of lower hemisphere is used.

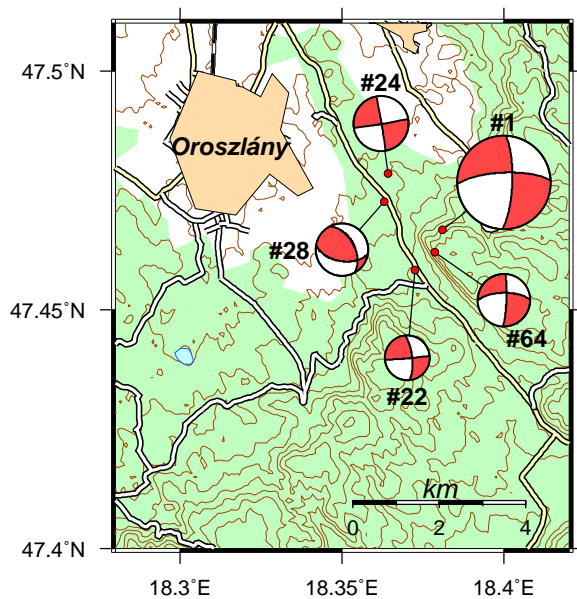


Figure 9: Source mechanisms of the Oroszlány mainshock (Event #1) and its four most significant aftershocks on a map of the source area. Event numbers are also indicated. Beachball size is proportional to event magnitude (shaded area: compression; open area: dilatation). Equal area projection of lower hemisphere is used. The color version of this figure is available only in the electronic edition.